Magnetocrystalline effects on the subsurface hydrogen diffusion in γ-Fe(001)

U.K. Chohan[a] , E. Jimenez-Melero[a,*], S.P.K. Koehler[b]

[a]*Materials Performance Centre, School of Materials, The University of Manchester, Manchester M13 9PL, UK*

[b]*School of Science and the Environment, Manchester Metropolitan University, Manchester M1 5GD, UK*

*Corresponding author.

Email: enrique.jimenez-melero@manchester.ac.uk

University of Manchester

School of Materials

Materials Performance Centre

Oxford Road

Manchester

M13 9PL

United Kingdom

Abstract

The effect of magnetism on hydrogen adsorption and subsurface diffusion through face-centred cubic (fcc) γ-Fe(001) was investigated using spin-polarised density functional theory (s-DFT). The non-magnetic (NM), ferromagnetic (FM), and antiferromagnetic single (AFM1) and double layer (AFMD) structures were considered. For each magnetic state, the hydrogen preferentially adsorbs at the fourfold site, with adsorption energies of 4.07, 4.12, 4.03 and 4.05 eV/H atom for the NM, FM, AFM1 and AFMD structures. A total barrier of 1.34, 0.90, 1.32 and 1.25 eV and a bulk-like diffusion barrier of 0.6, 0.2, 0.4 and 0.3 eV were calculated for the NM, FM, AFM1 and AFMD magnetic states. The Fe atoms nearest to the H atom exhibited a reduced magnetic moment, whereas the next-nearest neighbour Fe atoms exhibited a non-negligible local perturbation in the magnetic moment. The presence of magnetically ordered structures has a minimal influence on the minimum energy path for H diffusion through the lattice and on the adsorption of H atoms on the Fe(001) surface, but we computed a significant reduction of the bulk-like diffusion barriers with respect to the non-magnetic state of fcc γ-Fe.

Keywords: gamma iron; magnetism; density functional theory; hydrogen diffusion

1. Introduction

Austenitic steels are widely used in a range of technologies such as in nuclear power plants [1] and in offshore structures [2]. The face-centred cubic (fcc) austenite phase, i.e. γ-Fe, is stable at ~1185-1665 K [3-5], although it can be present in a metastable state at lower temperatures via the addition of Ni, Mn, C or N [6-8]. This phase is of particular interest due to its complex magnetic behaviour, with a reported value of the Néel temperature of T_N ~70 K [9]. Alloying elements can alter the magnetic ground state and the critical temperature of γ-Fe, since Ni is ferromagnetic below T_C = 631 K [10], whereas α-Mn adopts a complex non-collinear antiferromagnetic phase below T_N = 95 K [11]. The magnetic properties are of paramount importance in magnetoelectronics [12-15] and biomedicine [16-19], and also in steel components close to the D-T plasma of magnetically-confined fusion reactors [20-22]. Three magnetically ordered phases are considered in the collinear approximation used in theoretical studies: the ferromagnetic (FM-↑↑↑↑ ...) phase, as well as multi-layered anti-ferromagnetic phases, namely the single (AFM1-↑↓↑↓ ...) and double (AFMD-↑↑↓↓ ...) layer phases [23-26]. The double-layer structure has been reported to be energetically most favourable, and provides a reasonable approximation of the spin-spiral state with a propagation vector $\mathbf{k} \approx \frac{2\pi}{a}[001]$ [26-28], where a denotes the lattice parameter of the fcc crystal structure. The bulk magnetic ordering of γ-Fe extends to surface studies, in which γ-Fe films are grown on a Cu(100) substrate [9, 29, 30].

The magnetic ordering of Fe atoms in γ-Fe is rooted in the interaction of itinerant d-electrons. These electrons may be exchanged when interacting with interstitial atoms. Thus, the magnetic state of the metal may have an effect on the interstitial diffusion pathway and energetics of light atoms such as hydrogen through the metal. The presence of significant amounts of hydrogen in steels causes the material to become brittle over time, eventually

resulting in catastrophic failure. This phenomenon of hydrogen embrittlement (HE) in steels has been extensively studied since its discovery by Johnson in 1875 [31]. There are different mechanisms for HE that are posed and thoroughly reviewed [32-35]; the most commonly invoked mechanisms are Hydrogen Enhanced Localised Plasticity (HELP) [35-38] and Hydrogen Enhanced DEcohesion (HEDE) [39, 40]. These mechanisms apply to differing steels and environmental conditions, and sometimes a combination of them applies [38, 41-43]. Moreover, the presence of hydrogen in the structure may induce the formation of bcc/bct α' or hcp ε martensite phase, depending on the austenite stability [44]. H-vacancy interactions in fcc metals also reduce the vacancy energy of formation, and produce an increase of the vacancy concentration in a material by several orders of magnitude [45]. Open grain boundaries in non-magnetic fcc Fe, such as Σ11, offer additional H trapping sites and also provide diffusion pathways for H with an energy barrier of 0.7 eV based on DFT calculations [46]. The accumulation of hydrogen at those grain boundaries reduces the critical strain required to fracture the material. Unfortunately an overarching model of HE for all different steels and other advanced metallic systems is not yet present. A common factor in any particular mechanism is that hydrogen must absorb into the material, thus the stages that lead to absorption constitute the early stages in the HE process. The early stage of HE is a two-step process: (1) hydrogen adsorbs onto the surface, followed by (2) hydrogen diffusing into the bulk. The adsorption process consists of hydrogen occupying a minimum energy site on the metal surface, and at relatively high temperatures diffusion occurs predominantly by hydrogen moving in-between interstitial sites, from the surface into the bulk. Hydrogen atoms would most probably advance on a pathway close to or on the minimum energy path (MEP) for diffusion. However, for diffusion to occur, an initial energy barrier must be overcome, which is the activation energy for diffusion from the surface into subsurface layers. Likewise, for bulk diffusion, a different energy barrier

must be surmounted as H atoms move from one subsurface layer into the next. We extracted the MEP in this work from a series of density functional theory (DFT) calculations. A relatively large number of 2D reduced potential energy surfaces (PES) were calculated at selected depths through a metallic slab via multiple energy minimisation calculations, in which a single H atom was placed at multiple sites on a mesh grid, and the energy of the entire system was minimised. The lowest energy hydrogen positions for every depth calculated were connected to yield the MEP. More importantly, however, this grid method, which we have applied previously [47], yields not only the MEP, but the PES as a function of depth through the Fe slab; this makes the grid method computationally more expensive, but it has the added benefit of also delivering energies of the H-Fe system away from the MEP, and can hence show how likely it is – or not – for an H atom to diffuse through the bulk away from the MEP.

In this work, we have assessed the diffusion of hydrogen through the γ-Fe(001) surface comparatively in the four aforementioned magnetic states (NM, FM, AFM1 and AFMD), using density functional theory (DFT). The pathways and energy barriers for diffusion are for the first time compared between the four magnetic states. The influence of the diffusing hydrogen on the magnetic moments of iron was additionally studied, as well as the interlayer spacing, for each magnetic case.

2. Computational methodology

Density functional theory (DFT) was used to calculate potential energy surfaces (PESs) for the surface adsorption and diffusion into sub-surfaces of hydrogen on and through the (001) surface of γ-Fe. The non-magnetic (NM), ferromagnetic (FM), anti-ferromagnetic single (AFM1) and double (AFMD) layer magnetic states were considered for each surface. The FM, AFM1 and AFMD states were incorporated in the model using spin-polarisation, in the collinear approximation, whilst the NM state was modelled using non-spin polarised DFT. The Vienna ab

initio simulation package (VASP) was employed [48], and a plane-wave basis set with 3D periodic boundary conditions described electronic interactions. The projector augmented-wave (PAW) approximation described valence and core electronic interactions [49]. Exchange and correlation effects were added within the generalised-gradient approximation (GGA) via the Perdew-Burke-Erzenhof (PBE) functional [50].

The lattice parameters were calculated for each of the four magnetic cases using geometry optimisation calculations (Table S1). The bulk systems were minimised using the conjugate gradient method [51], with a force tolerance of 10^{-5} eV Å^{-1}. The energies of all atoms were converged to within 10^{-6} eV. A cutoff energy of 400 eV was found to sufficiently converge the total energy of the system. The Methfessel Paxton method of order $N = 1$ with width 0.1 eV was used to apply electronic smearing [52]. A seven Fe layer slab model was used to model the surface and bulk of γ-Fe. A (2 × 2) cell was applied in all calculations. The Monkhorst-Pack algorithm [53] with a grid size of 7×7×1 was applied. A vacuum spacing of 20Å provided sufficient total energy convergence. The three bottom layers were frozen to represent the bulk region below the surface, while the Fe atoms in the top four layers were allowed to relax. The interlayer relaxation was computed for the slabs via the relation:

$$\Delta_{ij} = \frac{d_{ij} - d_0}{d_0} \times 100\% \quad (1)$$

where d_{ij} is the interlayer spacing between layers i and j (where $j = i + 1$ and $i = 1, 2, 3$) and d_0 is the bulk interlayer spacing. Additionally, the surface energy, γ_E, was calculated via the relation:

$$\gamma_E = \frac{E_{slab} - nE_{bulk}}{2A} \quad (2)$$

where E_{slab} is the total energy of the H-free slab, E_{bulk} is the energy of a single bulk Fe atom, n the total number of atoms in the slab, and A is the cross-sectional area of the slab.

A large number of hydrogen positions were sampled within the simulated slab using a mesh grid. A quarter of the 2 × 2 surface unit cell was sampled, using a 6 × 6 uniform grid on the domain $x,y \in [0,0.5]$, in fractional coordinates; this effectively corresponds to 144 hydrogen positions for every layer parallel to the surface. This mesh was repeated at nine selected depths into the surface (i.e. towards the bulk). A single H atom was successively placed at each point on the mesh, such that 1296 positions were sampled in or just above our slab of size ~130 Å^3, i.e. sufficiently tight for these studies. The H atom was allowed to relax in the x and y directions, but not along z, for two reasons: 1) our aim was to represent the PES for a number of planes *parallel* to the interface; 2) allowing relaxation along z from a local maximum would drive the H atom towards a minimum, and hence not provide a true representation of the overall PES. All Fe atoms of the first four layers were also allowed to relax in the slab. The energies at each point, E, were calculated via the relation:

$$E = E_{\text{slab+H}} - E_{\text{slab}} - E_{\text{H}} \tag{3}$$

where $E_{\text{slab+H}}$ is the energy of the H-containing slab, and E_{H} is the ground state energy of a single free H atom in a 10 × 10 × 10 A^3 box. The energies were then calculated relative to the global minimum of the entire slab, which was set to zero energy.

Spin polarised partial density of states (PDOS) were calculated for each magnetic state. The spin polarised d-band widths, $w_d^{\pm}$, were calculated using the spin-up and spin-down density of states, D^+ and D^-, via the relation [54]:

$$w_d^{\pm} = \sqrt{\frac{\int_{-\infty}^{\infty} E^2 D^{\pm}(E)\mathrm{d}E}{\int_{-\infty}^{\infty} D^{\pm}(E)\mathrm{d}E}} \tag{4}$$

where $D^{\pm}$ is the spin-up and down PDOS, respectively. The overall d-band width, w_d, was thereupon derived by averaging according to:

$$w_d = \frac{1}{2}(w_d^+ + w_d^-) \quad (5)$$

3. Results and Discussion

3.1. Hydrogen-free (001) surface of γ-Fe

Four magnetic phases of γ-Fe were considered for the bulk structure, i.e. the NM, FM, AFM1 and AFMD cases, see Fig. 1. The lattice parameter, a, axial ratio, c/a, and the magnitude of the magnetic moment per Fe atom, $|\mu_{Fe}|$, were calculated using spin-polarised DFT. These quantities are all in agreement with previous literature values [23, 26]. Given the reasonable description of the bulk cases, we then moved on to describe the (001) surface of γ-Fe for each magnetic structure. We calculated the relaxation, surface energy and magnetic moment per Fe atom for each case, see Fig. 2. For the NM case, a contraction occurs in between the first two layers, i.e. $\Delta_{12} = -5.84\%$, which is compensated by an expansion in between the second and third layers of $\Delta_{23} = +3.60\%$. As a result, a smaller contraction is observed in between the third and fourth layers, namely $\Delta_{34} = -1.37\%$. For the FM case, a contraction of $\Delta_{12} = -1.18\%$ in between the first two layers was calculated, and an even smaller expansion between the second and third, and third and fourth layers. For the AFM1 case, we observe two very small contractions for the first two layer spacings, followed by a barely noticeable expansion between the third and fourth layer. For the AFMD case, all three interlayers displayed a contraction, i.e. $\Delta_{12} = -4.08\%$, $\Delta_{23} = -8.57\%$ and $\Delta_{34} = -3.33\%$. Clearly, the magnetic ordering of the Fe atoms impacts on the sign and magnitude of the interlayer relaxation. However, a discrepancy is present between the reported experimental data and our calculated values, with experiments demonstrating an expansion in all levels for FM fcc Fe thin films [30]. This difference, however, can be ascribed to the growth of fcc Fe films in the experiments occurring epitaxially on fcc Cu(100), in which the induced bcc→fcc transformation may result in localised stresses, whereas in our simulations we

use a pure Fe slab. The contraction observed in our calculations between the first two layers is expected for FM atoms due to the lowered coordination number, resulting in tighter binding between the first and second layers. There would then be a compensatory expansion in between the second and third layers. Similarly, the first two layers contract for all magnetic states. The reduction of the contraction manifested in the values of Δ_{12} for FM, AFM1 and AFMD relative to NM may be attributed to the magnetically reduced surface stress [55]. The presence of a free surface induces a higher magnetic pressure at the surface, leading to a normal force component on the surface Fe atoms in the direction of the magnetic moment [55]. This reduced surface stress state also decreases the surface energy with respect to the NM state. We calculated surface energies, γ_E, for the four magnetic states of 3.38, 2.27, 2.80 and 2.59 J m^{-2} for the NM, FM, AFM1 and AFMD states, respectively. The exchange interaction for opposing spin states between the surface and subsurface layers [56] may work to cancel this effect on the surface stress state, due to a switch in the sign in the magnetisation energy between the surface and subsurface Fe atoms according to the spin direction, which results in a lower "effective magnetic pressure" on the surface Fe atoms. This lowered magnetic pressure leads to the smaller reduction in both the interlayer relaxation and the surface energies for the AFM1 and AFMD cases relative to the FM case.

For all magnetic cases, the surface layer displays an enhanced magnetic moment, with respect to the bulk Fe moment, when averaged over all surface Fe atoms, with values of $\mu_1 = 2.67$, 2.29, 2.81 μ_B for the FM (bulk 2.42 μ_B), AFM1 (bulk 1.53 μ_B) and AFMD (bulk 2.24 μ_B) cases, respectively. These values drop close to the bulk values of the Fe magnetic moment already in the second layer. The *d*-band width, w_d, drops for all magnetic cases at the surface layer with respect to the bulk, see Table 1. This decrease in the *d*-band width is related to the lowering in the coordination number at the surface, resulting in an enhancement in the

localised states in the *d*-band in the Fe atoms [57]. This enhancement in the magnetic moment at the surface to a value of 2.85 μ_B has previously also been observed experimentally [58]. We have also reported an analogous effect in our previous DFT study of the (110) surface of ferromagnetic bcc α-Fe [59].

3.2. Magnetocrystalline effect on hydrogen adsorption and diffusion through γ-Fe

Mesh grids were placed at two different heights above the (001) surface to find the preferential adsorption sites of hydrogen for the four magnetic states. All three types of high symmetry adsorption sites were sampled, namely the on-top (ot), two-fold (2f) and four-fold (4f) sites. In all four magnetic cases, the 4f site was determined to be the preferential adsorption site. This site is in between four identical Fe atoms, and is characterised by a fourfold rotational symmetry. The adsorption energies (4.07, 4.12, 4.03 and 4.05 eV/H atom for the NM, FM, AFM1 and AFMD cases) do not vary significantly, and the magnetic state seems to only have a nominal effect on the adsorption energy of hydrogen on the surface. These results are in contrast with our recent DFT calculations on the non-magnetic (110) and (111) Fe surfaces, where the adsorbed H prefers to reside at either the short-bridge site or the threefold site, with adsorption energies of 3.92 eV and 4.05 eV, respectively [47].

The potential energy surfaces (PES) for diffusion were calculated via a series of energy minimisations, where a single hydrogen atom was placed on the intersections of a regular 6 × 6 mesh grid at nine selected depths (from the surface through to the fourth layer in half-layer intervals); the Fe atoms in the top four layers and the hydrogen atom were allowed to relax in the *xy* plane. This resulted in 324 individual geometry optimisations for each quarter of each layer and magnetic state, such that we determined the energy minimum at each depth. While we are not predicting whether the minima at each depth are minima or maxima along the MEP, it is a valid assumption that these extrema along the MEP are either in, or between the layers

containing Fe atoms (i.e. within the layers we are probing), such that we are confident not to miss any extrema. We obtained the MEP by connecting the position of the minima at each depth. While the nudged elastic band (NEB) method [60] may give a better representation of the MEP by probing a number of images between the minimum and maximum, our grid method has the added advantage of probing the energy landscape away from the MEP. A plot of the energies of these minima as a function of depth leads to the overall potential energy curves shown in Fig. 3. We note that while we have not calculated energies between the minima and maxima along the MEP as NEB would do, the energy variations in each separate layer in Fig. 3 allow us to conclude that the energy minima and maxima in our grid method are not out by more than 0.02 eV. A recent DFT study of hydrogen diffusion on 23 (non-magnetic) metal surfaces also concluded that the difference in estimation of the activation barrier based on the PES and the NEB profiles was less than 0.01 eV [61]. In the four cases reported in our work, a relatively large energy barrier is present for hydrogen entering from the surface to the first subsurface layer. This is expected, as the H-Fe chemisorption bond has to be broken. The initial penetration of the H atom into the Fe slab hence seems to be the rate-determining step. Once the H enters the subsurface, the energy barriers for the H atom passing from one layer to the next remain fairly constant for both the FM and AFM1 magnetic cases. Crucially, this is not the case for the AFMD case, which is likely due to the switch in the spin direction between the first and second (same), and third and fourth layers. We found that the hydrogen atom tends to diffuse from one octahedral site to the next. This is in excellent agreement with the recent neutron diffraction work by Machida *et al.*, who experimentally identified the octahedral sites within non-magnetic fcc iron crystals as the preferential sites for deuterium atoms, whereas the minor occupation of tetrahedral sites occurs by interstitial thermally-driven diffusion of deuterium atoms along the <111> direction [62]. However, in addition to the experimental work, our DFT calculations

show that the preference for diffusion along the octahedral sites persists for all magnetic cases, with only marginally different diffusion pathways for the four systems; this shows that the magnetism does not have a noticeable effect on the exact MEP for diffusion, see Fig. 4a. On the other hand, magnetism does have a significant influence on the energy barriers for diffusion. The *surface-to-subsurface* diffusion barrier, i.e. the initial step from the surface to the first sub-surface layer, is 1.34, 0.90, 1.32 and 1.25 eV for the NM, FM, AFM1 and AFMD states, respectively. Thus, the H atom may enter from the surface into sub-surfaces for the FM case with relative ease. The *bulk-like* diffusion barriers for hydrogen were found to be 0.6, 0.2, 0.4 and 0.3 eV for the NM, FM, AFM1 and AFMD states, respectively. The experimental value of the activation energy for bulk diffusion, based on tritium injection and diffusion in non-magnetic SUS-316 austenitic stainless steel with a clean surface, was reported to be ~0.66eV [63]. Earlier experimental work on the permeation and diffusion of hydrogen and deuterium in 310 austenitic stainless steel yielded a value for the bulk energy barrier for diffusion of ~0.5eV [64]. Our estimated value of 0.6 eV for H bulk diffusion in the NM case lies close and in between the experimental values reported for non-magnetic SUS-316 and 310 austenitic steels, ~0.66 eV and ~0.5 eV respectively. This provides confidence in our grid methodology not over- or underestimating the energy barrier for H diffusion in fcc Fe. Furthermore, recently DFT calculations derived a value of ~0.35eV for bulk H diffusion in AFMD fcc Fe [65], which is close to our estimated value of 0.3 eV for the AFMD case. Our novel comparative DFT results considering the four aforementioned magnetic states have implications for the hydrogen embrittlement (HE) of Fe-based alloys. If an austenitic alloy was selected which may have ferromagnetic ordering of the Fe atoms, then the H atoms may very readily diffuse through the surface and into the bulk. As a result, ferromagnetic alloys appear to be more susceptible to

hydrogen embrittlement as compared to the antiferromagnetic, and even more when compared to non-magnetic states.

As the hydrogen diffuses through the metallic lattice, electrons in the *s* orbital of H atoms interact with the itinerant *d* electrons of Fe. This is a two-way process, thus an effect on the local Fe magnetism is observed as the fingerprint of hydrogen diffusion into and through the fcc Fe lattice. The hydrogen has four minima as it passes from the surface to the fourth layer, all corresponding to octahedral sites. The H atom causes a local reduction in the magnetic moment in the nearest Fe atoms, and this shift in magnetic moment has a "cascade" effect on the next layer below, as shown in Fig. 4b-d. This is observed as a local reduction in the magnetic moment on two Fe atoms and an asymmetric reduction in the magnetic moment of two further Fe atoms. It was noted that the average of the four values of the magnetic moment in the second layer value has an identical value to the magnetic moment for the Fe atoms in the second layer of the H-free slab, for each magnetic case. Therefore, the H atom induces a perturbation in the exchange interaction of itinerant *d* electrons between the Fe atoms in the second layer, though it does not induce a net electron transfer towards the H atom, likely due to shielding effects from the surface layer by the electrons which transferred from the nearest-neighbour Fe atoms. Recent DFT calculations have also reported a reduction in the magnetic moment of only the nearest-neighbour Fe atoms in an Fe_3 cluster immersed in a Cu(111) surface, due primarily to an increased population of minority spin *d* states near the Fermi level [66]. Interstitial H atoms are also over screened by the charge transfer from their nearest neighbour atoms in ferromagnetic fcc Ni; in this case, new H-induced electronic states mainly due to 1s–3d hybridization appear at ~10 eV below the Fermi level [67]. It is to be noted that only a single H atom is diffusing through the slab in our DFT simulations, therefore any observed effects on the magnetic moments are expected to be relatively small. However, local effects are clearly observed in our

DFT calculations. These local effects are investigated via tracing shifts in the *d*-band width by computing w_d for a specific single Fe atom belonging to the surface layer as the H atom diffuses through the slab, see Table 2. The w_d value was calculated for a surface Fe atom, as the H atom occupies successively each of the minimum positions illustrated in Fig. 4. The *d* band width w_d varies by a small amount for every magnetic state. In general, the w_d value decreases from the first minimum to the last. The reduction corresponds to an enhancement in the magnetic moment as explained earlier. Therefore, the presence of hydrogen near an Fe atom results in a reduction in the magnetic moment. The variation in values in-between also generally corresponds to the enhancement (decreased w_d) or reduction (increased w_d) in the magnetic moment. When the H atom is at the fourth minimum position (i.e. furthest away from the surface in our simulations), then both the magnetic moment $|\mu|$ and the *d* band width w_d of the surface Fe atom approach the values of the surface Fe atom in the H-free slab for each magnetic state; this is likely due to shielding of the surface layer by the electron transfer primarily with the nearest-neighbour Fe atoms.

4. Conclusions

We investigated the mutual interplay between the local Fe magnetism and the diffusion of H atoms through γ-Fe(001) using spin-polarised density functional theory (s-DFT). Four magnetic configurations were considered, namely the non-magnetic (NM), ferromagnetic (FM), and antiferromagnetic single (AFM1) and double-layer (AFMD) structures. The fourfold site was found to be the preferential adsorption site for each magnetic state, with a minimal effect of the magnetic ordering on the H adsorption energies. Equally, we observed only a negligible influence of the magnetic state on the actual MEP as the H atom diffuses from one octahedral site to the next. However, and overall barrier of 1.34, 0.90, 1.32 and 1.25 eV (for the NM, FM, AFM1 and AFMD magnetic states) and a *bulk-like* diffusion barrier of 0.6, 0.2, 0.4 and 0.3 eV

were calculated, respectively; this demonstrates a relatively large influence of the magnetic ordering on the diffusion energies. Furthermore, the H atom reduces the magnetic moment of the nearest neighbour Fe atoms, whilst causing perturbations in the exchange interaction of itinerant *d* electrons of Fe atoms in the next-nearest neighbour sites. This study demonstrates the significant effect that magnetic ordering exerts on diffusion of hydrogen, which may increase the susceptibility of magnetic austenitic Fe alloys to hydrogen embrittlement. It appears that in order to reduce the chances of HE, structural components should be fabricated preferentially from non-magnetic austenitic steels.

Acknowledgements

We would like express our appreciation to the Engineering and Physical Sciences Research Council UK via the Centre for Doctoral Training in Advanced Metallic Systems for their financial support (EP/L016273/1). We thank the Dalton Cumbrian Facility, partly funded by the Nuclear Decommissioning Authority, for funding the cost of computational time.

References

[1] K.L. Murty, I. Charit, Structural materials for Gen-IV nuclear reactors: Challenges and opportunities, J. Nucl. Mater 88 (2008) 189-195.

[2] M.S. Han, S.K. Jang, S.J. Kim, Investigation on SCC and HE of STS 304 austenitic stainless steel for offshore structures, Rare Metals 30 (2011) 633-638.

[3] D.A. Young, *Phase diagrams of the elements* (Lawrence Livermore Lab, California Univ., 1975).

[4] O.L. Anderson, Properties of iron at the Earth's core conditions, Geophys. J. Int. **84** (1986) 561-579.

[5] C.S. Yoo, J. Akella, A.J. Campbell, H.K. Mao, R.J. Hemley, Phase diagram of iron by in situ X-ray diffraction: implications for Earth's core, Science 270 (1995) 1473-1474.

[6] P.S. Korinko, S.H. Malene, Considerations for the weldability of types 304L and 316L stainless steel, J. Fail. Anal. Prev. 1 (2001) 61-68.

[7] L.M. Guerrero, P. La Roca, F. Malamud, A. Baruj, M. Sade, Composition effects on the fcc-hcp martensitic transformation and on the magnetic ordering of the fcc structure in Fe-Mn-Cr alloys, Mater. Des. 116 (2017) 127-135.

[8] T. Maki, Ferrous shape memory alloys, in *Shape memory materials*, edited by K. Otsuka and C. M. Wayman, pp. 117–132, Cambridge University Press, Cambridge, 1999.

[9] Y. Tsunoda, S. Imada, N. Kunitomi, Anomalous lattice contraction and magnetism of γ-Fe precipitates in Cu, J. Phys. F 18(7) (1988) 1421-1431.

[10] B. Legendre, M. Sghaier., Curie temperature of nickel, J. Therm. Anal. Calorim. **105**(1) (2011) 141-143.

[11] D. Hobbs, J. Hafner, D. Spišák, Understanding the complex metallic element Mn. I. Crystalline and noncollinear magnetic structure of α-Mn, Phys. Rev. B. **68** (2003) 014407(1)-014407(18).

[12] G. A. Prinz, Magnetoelectronics, Science 282 (1998) 1660-1663.

[13] G. A. Prinz, Magnetoelectronics applications, J. Mag. Mag. Mater 200(1) (1999) 57-68.

[14] C. Binek, B. Doudin, Magnetoelectronics with magnetoelectrics, J. Phys. 17(2) (2004) L39.

[15] B.G.E. Brataas, A.P.J. Kelly, Non-collinear magnetoelectronics, Phys. Rep 427(4) (2006) 157-255.

[16] Q.A. Pankhurst, J. Connolly, S.K. Jones, J.J. Dobson, Applications of magnetic nanoparticles in biomedicine, J. Phys. D. 36(13) (2003) R167.

[17] B. Alemán, R. Ranchal, V. Reguero, B. Mas, J.J. Vilatela, Carbon nanotube fibers with martensite and austenite Fe residual catalyst: room temperature ferromagnetism and implications for CVD growth, J. Mater. Chem. C. 5(22) (2017) 5544-5550.

[18] H.B. Na, I.C. Song, T. Hyeon, Inorganic nanoparticles for MRI contrast agents, Adv. Mater. 21 (2017) 2133-2148.

[19] S. Behrens, Preparation of functional magnetic nanocomposites and hybrid materials: recent progress and future directions, Nanoscale 3(3) (2011) 877-892.

[20] V.D. Pustovitov, F. Villone, Effect of ferromagnetic structures on RWM growth rates: a cylindrical model and a verification on JET. Plasma Phys. Control. Fusion 52 (2010) 065010(1)-065010 (11).

[21] R. Fitzpatrick, Influence of ferromagnetic walls on resistive wall mode stability in tokamaks. Plasma. Phys. Control Fusion 56(10) (2014) 105002.

[22] X. Ji, N. Yanagi, T. Goto, H. Tamura, J. Miyazawa, A. Sagara, S. Wang, M. Qi, Y. Song, Investigation on the magnetic field distortion by ferromagnetism of the blanket for the helical fusion reactor. Fusion Eng. Des. 125 (2017) 631-634.

[23] N.I. Medvedeva, D. Van Aken, J.E. Medvedeva, Magnetism in bcc and fcc Fe with carbon and manganese, J. Phys. Condens. Matter. **22** (2010) 316002(1)-316002(7).

[24] P. M. Marcus, V.L. Moruzzi, S.L. Qiu, Tetragonal equilibrium states of iron, Phys. Rev. B 60(1) (1999) 369-372.

[25] D.W. Boukhvalov, Y.N. Gornostyrev, M.I. Katsnelson, A.I. Lichtenstein, Magnetism and local distortions near carbon impurity in γ-iron, Phys. Rev. Lett. 99(24) (2007) 247205(1)-247205(4).

[26] D. Spišák, J. Hafner, Complex reconstruction of γ-iron multilayers on Cu (100): Ab initio local-spin-density investigations, Phys. Rev. B 61(23) (2000) 16129-16136.

[27] O.N. Mryasov, V.A. Gubanov, A.I. Liechtenstein, Spiral-spin-density-wave states in fcc iron: Linear-muffin-tin-orbitals band-structure approach, Phys. Rev. B. 45(21) (1992) 12330-12336.

[28] Y. Tsunoda, Spin-density wave in cubic γ-Fe and γ-$Fe0_{100-x}$ Cox precipitates in Cu, J. Phys. 1 (1989) 10427-10438.

[29] S. Müller, P. Bayer, C. Reischl, K. Heinz, B. Feldmann, H. Zillgen, M. Wuttig, Phys. Rev. Lett. 74(5) (1995) 765-769.

[30] K. Heinz, S. Müller, L. Hammer, Crystallography of ultrathin iron, cobalt and nickel films grown epitaxially on copper, J. Phys. 11 (1999) 9437-9454.

[31] W.H. Johnson, On some remarkable changes produced in iron and steel by the action of hydrogen and acids, Nature 11(281) (1875) 393.

[32] S. Lynch, Mechanisms of hydrogen assisted cracking–a review, in *Hydrogen Effects on Material Behaviour and Corrosion Deformation Interactions*, edited by N.R. Moody, A.W. Thompson, R.E. Ricker, G.S. Was, R.H. Jones, pp. 449–466, The Minerals, Metals and Materials Society, Pennsylvania, 2003.

[33] D. Tromans, On surface energy and the hydrogen embrittlement of iron and steels, Acta Metall. Mater. 42 (1994) 2043-2049.

[34] M. Nagumo, T. Yagi, H. Saitoh, Deformation-induced defects controlling fracture toughness of steel revealed by tritium desorption behaviors. Acta Mater. 48 (2000) 943-951.

[35] C. Beachem, A new model for hydrogen-assisted cracking (hydrogen "embrittlement"), Metall. Trans. 3(2) (1972) 441-455.

[36] H. Birnbaum, Illinois University Report No. ADA208210, 1989 (unpublished).

[37] H. Birnbaum, P. Sofronis, Hydrogen-enhanced localized plasticity - a mechanism for hydrogen-related fracture, Mat. Sci. Eng. A 176 (1994) 191-202.

[38] S. Lynch, Environmentally assisted cracking: overview of evidence for an adsorption-induced localised-slip process, Acta Metall. 36(10) (1988). 2639-2661.

[39] J. Morlet, H. Johnson, and A. Troiano, *A new concept of hydrogen embrittlement in steel* (Wright Air Development Center, Ohio, 1957).

[40] C. McMahon, Hydrogen-induced intergranular fracture of steels, Eng. Fract. Mech. 68(6) (2001) 773-788.

[41] S. Lynch, Hydrogen embrittlement phenomena and mechanisms, Corros. Rev. 30 (2012) 105-123.

[42] M. Djukic, V. Zeravcic, G. Bakic, A. Sedmark, B. Rajicic, Hydrogen embrittlement of low carbon structural steel, Procedia Mater. Sci. 3 (2014) 1167-1172.

[43] A. Nagao, C. Smith, M. Dadfarnia, P. Sofronis, I. Robertson, The role of hydrogen in hydrogen embrittlement fracture of lath martensitic steel, Acta Mater. 60(13) (2012) 5182-5189.

[44] P. Rozenak, L. Zevin, D. Eliezer, Hydrogen effects on phase transformations in austenitic stainless steels. J. Mater. Sci. 19 (1984) 567-573.

[45] R. Nazarov, T. Hickel, J. Neugebauer, Ab initio study of H-vacancy interactions in fcc metals: Implications for the formation of superabundant vacancies, Phys. Rev. B 89 (2014) 144108(1)- 144108(18).

[46] Y.A. Du, L. Ismer, J. Rogal, T. Hickel, J. Neugebauer, R. Drautz, First-principles study on the interaction of H interstitials with grain boundaries in α- and γ –Fe, Phys. Rev. B 84 (2011) 144121(1)- 144121(13).

[47] U.K. Chohan, S.P.K. Koehler, E. Jimenez-Melero, Diffusion of hydrogen into and through γ-iron by density functional theory, Surf. Sci. 672-673 (2018) 56-61.

[48] G. Kresse, J. Furthmüller, Efficiency of ab-initio total energy calculations for metals and semiconductors using a plane-wave basis set, Comp. Mater. Sci. **6**(1) (1996) 15-50.

[49] P.E. Blöchl, Projector augmented-wave method, Phys. Rev. B. 50 (1994) 17953-17979.

[50] J.P. Perdew, K. Burke, M. Ernzerhof, Generalized Gradient Approximation Made Simple, Phys. Rev. Lett. 77(18) (1996) 3865-3868.

[51] M.C. Payne, M.P. Teter, D.C. Allan, T.A. Arias, J.D. Joannopoulos, Iterative minimization techniques for ab initio total-energy calculations: molecular dynamics and conjugate gradients, Rev. Mod. Phys 64(4) (1992) 1070-1072.

[52] M.P.A.T. Methfessel, A.T. Paxton, High-precision sampling for Brillouin-zone integration in metals, Phys. Rev. B 40(6) (1989) 3616-3621.

[53] J.D. Pack, H.J. Monkhorst, Special points for Brillouin-zone integrations, Phys. Rev. B 13(12) (1976) 5188-5192.

[54] P. Kratzer, B. Hammer, J. No, A theoretical study of CH_4 dissociation on pure and gold-alloyed Ni (111) surfaces, J. Chem. Phys. 105(13) (1996) 5595-5604.

[55] M.P. Punkkinen Q.M. Hu, S.K. Kwon, B. Johansson, J. Kollár, L. Vitos, Surface properties of 3d transition metals, Phil. Mag. 91(27) (2011) 3627-3640.

[56] Y.M. Zhou, D.S. Wang, Y. Kawazoe, Effective ab initio exchange integrals and magnetic phase transition in fcc Fe and Mn antiferromagnets, Y. Kawazoe, Phys. Rev. B. 59(13) (1999) 8387-8390.

[57] H. Lüth, *Solid surfaces, interfaces and thin films* (Springer, Berlin, 2001).

[58] C.L. Fu, A.J. Freeman, Electronic and magnetic properties of the fcc Fe (001) thin films: Fe/Cu (001) and Cu/Fe/Cu (001), Phys. Rev. B. 35(3) (1987) 925-932.

[59] U.K. Chohan, E. Jimenez-Melero, S.P.K. Koehler, Surface atomic relaxation and magnetism on hydrogen-adsorbed Fe (110) surfaces from first principles, Appl. Surf. Sci 387 (2016) 385-392.

[60] H. Jónsson, G. Mills, K. W. Jacobsen, ‘‘Nudged elastic band method for finding minimum energy paths of transitions,’’ in Classical and Quantum Dynamics in Condensed Phase Simulations, edited by B.J. Berne, G. Ciccotti, and D. F. Coker, World Scientific, Singapore, 1998, p. 385-404.

[61] L. Kristinsdóttir, E. Skúlason, A systematic DFT study of hydrogen diffusion on transition metal surfaces, Surf. Sci. 606 (2012) 1400–1404.

[62] A. Machida, H. Saitoh, H. Sugimoto, T. Hattori, A. Sano-Furukawa, N. Endo, Y. Katayama, R. Iizuka, T. Sato, M. Matsuo, S. Orimo, K. Aoki, Site occupancy of interstitial deuterium atoms in face-centred cubic iron, Nature Mater. 5 (2014) 5063(1)-5063(6).

[63] M. Sugisaki, H. Furuya, H. Ueki, S. Ejima, Surface reaction and bulk diffusion in SUS-316 stainless steel, J. Nucl. Mater. 133-134 (1985) 280-283.

[64] N.R. Quick, H.H. Johnson, Permeation and diffusion of hydrogen and deuterium in 310 stainless steel, 472 K to 779 K, Metall. Trans. A 11A (1979) 67-70.

[65] T. Hickel, R. Nazarov, E.J. McEniry, G. Leyson, B. Grabowski, J. Neugebauer, Ab Initio Based Understanding of the Segregation and Diffusion Mechanisms of Hydrogen in Steels, JOM 66 (2014) 1399-1405.

[66] P.F. Bessarab, V.M. Uzdin, H. Jónsson, Effect of hydrogen adsorption on the magnetic properties of a surface nanocluster of iron, Phys. Rev. B 88 (2013) 214407(1)- 214407(8).

[67] A. León, E.A. Velásquez, J. Mazo-Zuluaga, J.Mejía-López, J.M.Florez, P.Vargas, Magnetic effects of interstitial hydrogen in nickel, J. Magn. Magn. Mater. 421(2017) 7–12.

[68] T. Kraft, P.M. Marcus, M. Scheffler, Atomic and magnetic structure of fcc Fe/Cu (100), Phys. Rev. B 49(16) (1994) 11511-11514.

[69] G.W. Fernando, B.R. Cooper, Theory of electronic structure and magnetic behavior of fcc iron grown on Cu (001), Phys. Rev. B. 38(5) (1988) 3016-3027.

[70] T. Shimada, Y. Ishii, T. Kitamura, Ab initio study of magnetism at iron surfaces under epitaxial in-plane strain, Phys. Rev. B. 81(3) (2010) 134420(1)-134420(7).

[71] H. Chamati, N.I. Papanicolaou, Y. Mishin, D.A. Papaconstantopoulos, Embedded-atom potential for Fe and its application to self-diffusion on Fe (100), Surf. Sci. 600(9) (2006) 1793-1803.

[72] J. Yu, X. Lin, J. Wang, J. Chen, W. Huang, First-principles study of the relaxation and energy of bcc-Fe, fcc-Fe and AISI-304 stainless steel surfaces, Appl. Surf. Sci. 255(22) (2009) 9032-9039.

[73] J.P. Hirth, *Theory of Dislocations* (Wiley, New York, 1982).

[74] T. Asada, S. Blügel, Total energy spectra of complete sets of magnetic states for fcc-Fe films on Cu (100), Phys. Rev. Lett. 79(3) (1997) 507-510.

[75] M. Aldén, H.L. Skriver, S. Mirbt, B. Johansson, Surface energy and magnetism of the 3d metals, Surf. Sci. 315 (1994) 157-172.

Tables

Table 1. The *d*-band width, w_d, computed for the clean surfaces for different spatial orbital contributions for all magnetic states, at the surface and bulk layers.

Magnetic state	Layer	*d*-band width, w_d/eV					
		d_{xy}	d_{yz}	d_{z^2}	d_{xz}	$d_{x^2-y^2}$	Average
FM	Surface	2.26	2.33	2.36	2.37	2.80	2.42
	Bulk	2.31	2.72	2.34	2.57	2.79	2.55
AFM1	Surface	2.14	2.03	2.01	2.06	2.14	2.08
	Bulk	2.23	2.32	2.17	2.37	2.36	2.29
AFMD	Surface	2.07	1.96	1.98	1.89	2.03	1.99
	Bulk	2.14	2.24	2.08	2.20	2.19	2.17

Table 2. The average *d*-band width, w_d, computed for H at the four minimum positions for the FM, AFM1 and AFMD cases. The magnetic moments of a surface Fe atom are in brackets. The H-free surface value is provided as a reference value.

Magnetic state	*d*-band width, w_d/eV (Surface magnetic moment, μ_1/μ_B)				
		Minima index			
	H-free surface	1	2	3	4
FM	2.42 (2.67)	2.49 (2.67)	2.44 (2.72)	2.42 (2.68)	2.40 (2.68)
AFM1	2.08 (2.29)	2.15 (2.32)	2.10 (2.34)	2.10 (2.27)	2.07 (2.28)
AFMD	1.99 (2.81)	2.00 (2.70)	2.04 (2.83)	1.94 (2.76)	1.98 (2.81)

Figures

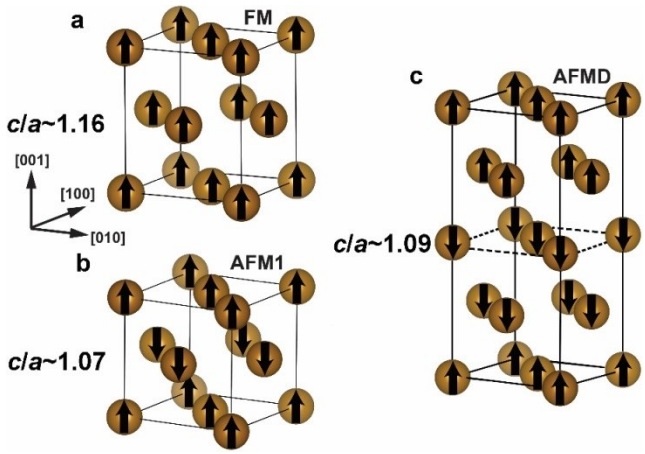

Fig. 1. The bulk γ-Fe unit cells for the three magnetic cases: (a) ferromagnetic (FM), (b) antiferromagnetic single- (AFM1) and (c) double layer (AFMD) structures. The axial ratio *c/a* is listed for each case, where *c* is magnitude of the crystallographic *z* axis. The arrows indicate the direction of the magnetic moment on each Fe atom.

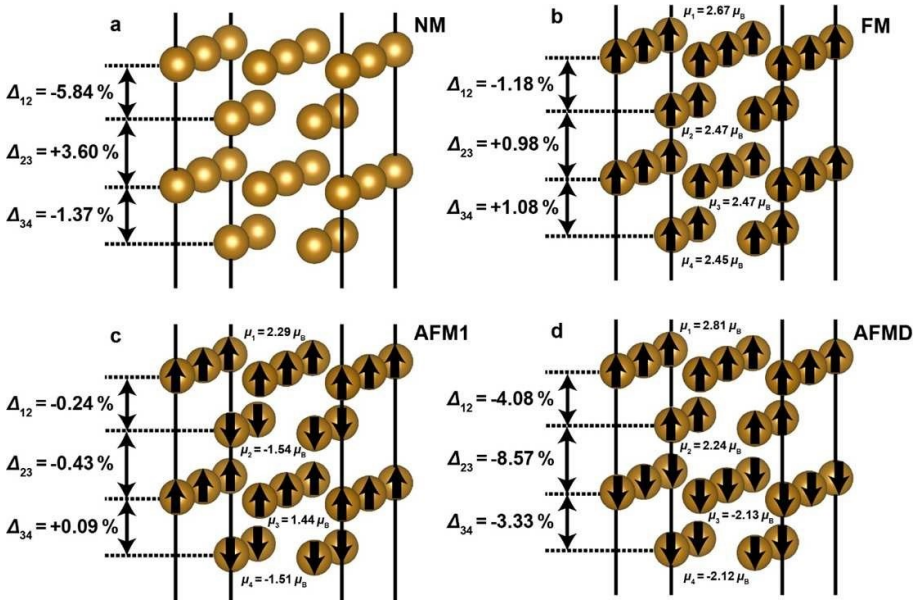

Fig. 2. The (2 × 2) γ-Fe cell surfaces for the: (a) NM, (b) FM, (c) AFM1 and (c) AFMD structures. The arrows indicate the direction of the magnetic moment on each Fe atom, and the average magnetic moment per Fe atom, μ_i, for each layer *i* is given. The interlayer relaxation Δ_{ij} (for $j = i + 1$ and $i = 1,2,3$) in between the top four layers is indicated. Only the four relaxing layers are displayed.

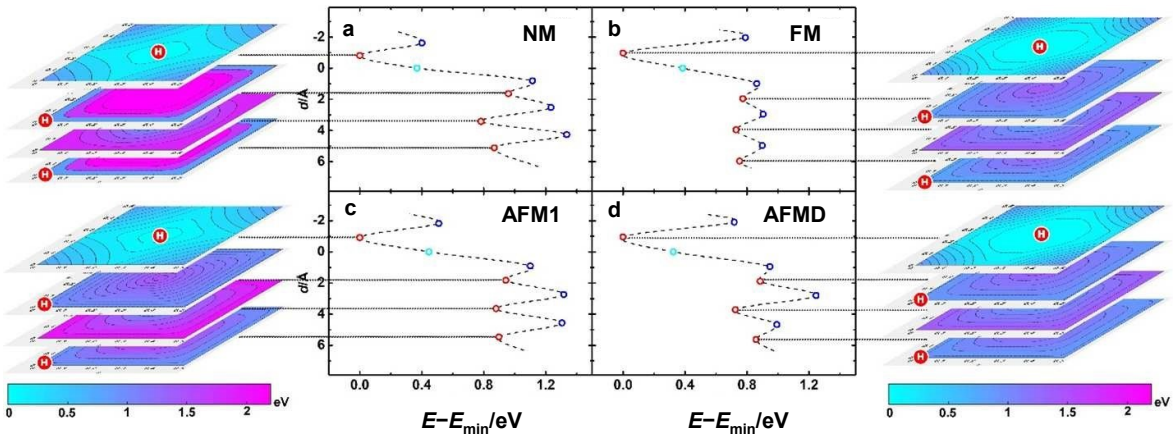

Fig. 3. The 2D potential energy surface at local minima and energy profile for hydrogen diffusion through the surface for (a) NM, (b) FM, (c) AFM1 and (d) AFMD cases. The dotted line between stationary points is only a guide to the eye.

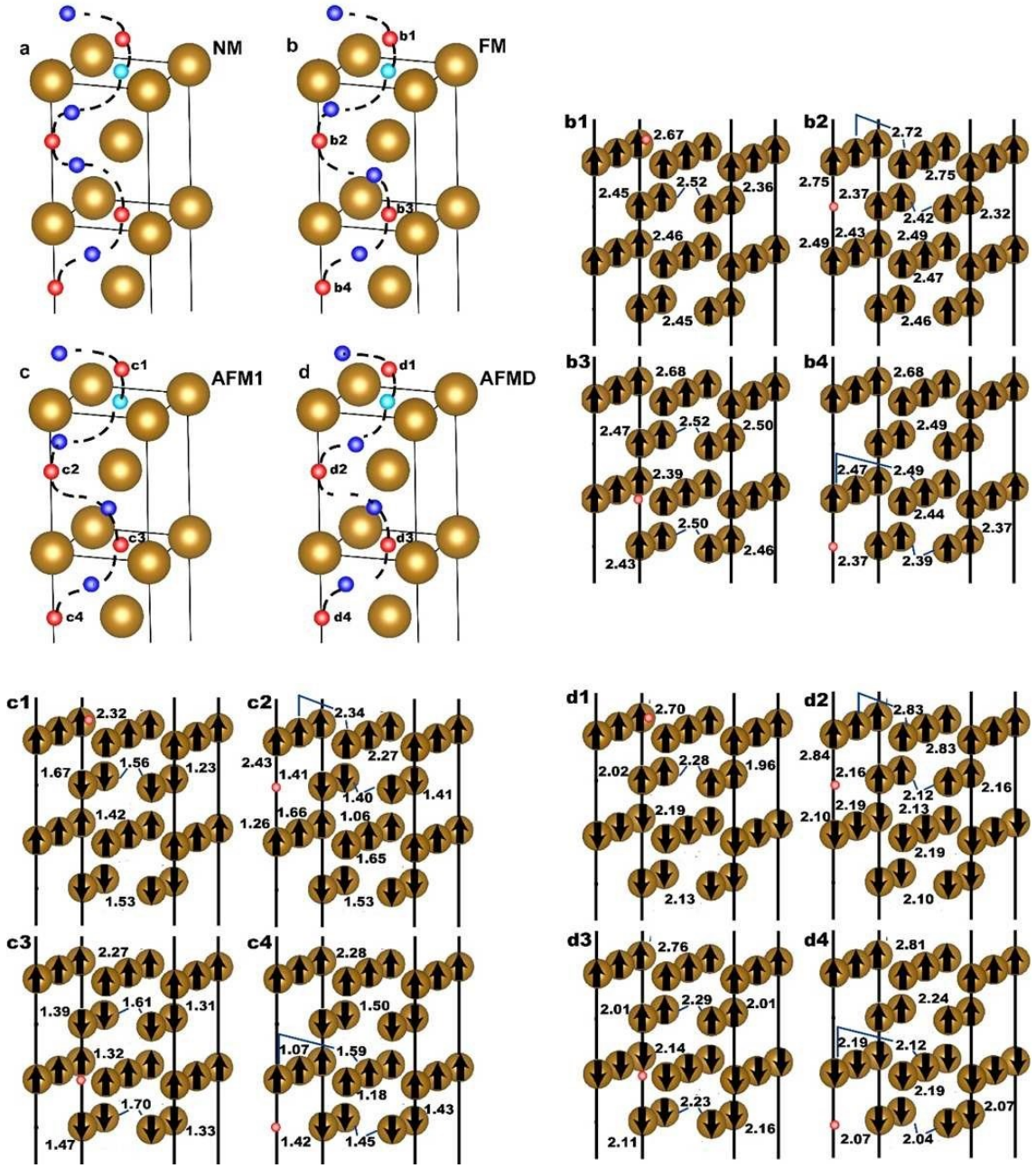

Fig. 4. The minimum energy path (MEP) for hydrogen diffusion through the (001) surface of γ-Fe for the (a) NM, (b) FM, (c) AFM1 and (d) AFMD cases. The dotted line is a guide to the eye. For each magnetic case, the four minima positions for the H atom are labelled 1-4 according to the corresponding figure index (a-d), with corresponding sketches of the four layer (2 × 2) slab for each given minima, with the magnitude of the magnetic moments on each Fe atom indicated. The direction of the magnetic moment is signified. A single value for any given layer indicates all the Fe atoms have that particular magnetic moment in that layer.